Supplementary information

Remarkable heat conduction mediated by non-equilibrium phonon polaritons

In the format provided by the
authors and unedited

Supplementary Information

for

Remarkable heat conduction mediated by non-equilibrium phonon polaritons

Zhiliang Pan, Guanyu Lu, Xun Li, James McBride, Rinkle Juneja, Mackey Long, Lucas Lindsay, Joshua D. Caldwell, and Deyu Li*

*Corresponding author: deyu.li@vanderbilt.edu

This file includes:

Additional theoretical simulation information
Sample preparation for thermal measurements
Uncertainty analysis
Thermal data summary
Additional optical results
Figs. S1 to S22
Tables S1 to S2
Supplementary information references

Additional theoretical simulation information

We solved radius- and branch-dependent electromagnetic waveguide equations for SPhP dispersions and attenuations appropriate for nanowire boundary conditions. The frequency-dependent complex wavevector, k, is calculated separately for surface modes supported in the Reststrahlen band[52-54]:

$$p_1^2 p_2^2 \left(p_2 \varepsilon_1 \frac{I_n'(p_1 a)}{I_n(p_1 a)} - p_1 \varepsilon_2 \frac{K_n'(p_2 a)}{K_n(p_2 a)} \right) \left(p_2 \frac{I_n'(p_1 a)}{I_n(p_1 a)} - p_1 \frac{K_n'(p_2 a)}{K_n(p_2 a)} \right) = (\varepsilon_2 - \varepsilon_1)^2 \left(\frac{nkk_0}{a} \right)^2, \qquad (S1)$$

and bulk modes supported outside the Reststrahlen band[54,55]:

$$\left[\frac{1}{p_2} \frac{H_n'(ip_2 a)}{H_n(ip_2 a)} - \frac{1}{p_1} \frac{J_n'(ip_1 a)}{J_n(ip_1 a)} \right] \left[\frac{\varepsilon_2}{p_2} \frac{H_n'(ip_2 a)}{H_n(ip_2 a)} - \frac{\varepsilon_1}{p_1} \frac{J_n'(ip_1 a)}{J_n(ip_1 a)} \right] = -\left(\frac{nk}{ak_0} \right)^2 \left(\frac{1}{p_1^2} - \frac{1}{p_2^2} \right)^2, \qquad (S2)$$

where I_n, K_n, H_n, and J_n are modified Bessel functions of the first and second kinds, Hankel function of the first kind, and Bessel function of the first kind, respectively, with branch n ($n = 0,1,2 ...$). The primes indicate derivatives with respect to the arguments. Radial wavevectors are $p_m = \sqrt{k^2 - \varepsilon_m k_0^2}$, ε_m is the permittivity for medium m ($m = 1,2$), $k_0 = \omega/c$, c is the speed of light, ω is the polariton frequency, i is the imaginary unit, and a is the nanowire radius. Note that for $n = 0$, Eqs. (S1) and (S2) reduce to Eq. (4) in the method section of the main text.

The $n = 0$ SPhP branch dispersion, as shown in Extended Data Fig. 1, differs significantly from the free-space light line, indicating a large momentum mismatch with far-field radiation and thus strong confinement to the nanowire. The higher branches are independent of radius and follow closely to the free-space light line. This is consistent with previous studies[53]. We note that in our measurements, the polaritons are thermally excited along the entire interface between the Au pad and SiC nanowire. The excited polaritons must first propagate along the Au-coated SiC nanowire to the end of Au-coated portion to contribute to the thermal conductivity of the uncoated, suspended wire segment. As such, we believe that the polariton contribution to thermal transport mainly comes from polaritons of the $n = 0$ branch, as the electromagnetic field of these polaritons is mainly confined in the SiC nanowires and can thus propagate along the Au-coated SiC nanowire. This understanding is supported by the dispersion curve where the $n = 0$ mode is beyond the light line of SiC, indicating polaritons of $n = 0$ modes are mainly propagating within the SiC. For higher order modes ($n \geq 1$), the fact that their dispersions are very close to the free-space light line indicates that these modes can only exist at the interface between SiC and free space and cannot propagate along the Au-SiC interface. Therefore, we only consider the $n = 0$ branch SPhPs for thermal transport.

In addition, Fig. S3 demonstrates the radius dependence of calculated G (Eq. 1 of the main text). Within the range of radius of our measured samples (24 – 39 nm), the change of thermal conductance is less than 20%. Thus, the effect of varying sample radius does not impact the conclusions presented in the main text.

Sample preparation for thermal measurements

The conventional micro-thermal bridge device (Fig. S4a) has 4 inner Pt electrodes for 4-point electrical measurements. To exclude direct contacts between SiC nanowires and any metal launcher except the coated Au layer, the inner Pt electrodes were removed using focused ion beam (Fig. S4b) and all SiC nanowires were in direct contact with a 200 nm thick SiO_2 layer deposited and patterned on the suspended membranes.

Samples with Au coating at the end were prepared following the procedure shown in Fig. S5. A SiC nanowire was placed to the edge of a piece of PDMS, with a few microns extending out from

the edge. Thin MoO_3 flakes were placed on the wire to cover the portion sitting on the PDMS surface. Au sputtering was performed on both sides of the exposed wire segment. Then the MoO_3 flakes covering the nanowire were removed and the wire sample was retrieved for subsequent thermal measurements. All sample manipulation were carried out under an optical microscope mounted with a long working distance (6.5 mm), high magnification (100x) objective lens using a sharp tungsten probe mounted on an in-house built micromanipulator.

Next, the SiC nanowire was transferred from the PDMS surface to the thermal measurement device using a sharp probe. Extreme care was taken to guarantee that the suspended lengths in bare wire measurements and the Au-coated sample measurements were approximately the same at a given gap distance. For Au-coated samples, the Au-coated portion(s) was(were) sitting on the SiO_2 layer of the suspended membrane, with less than 200 nm protruding from the edge so that the Au-coated portion is within the heat source/sink and not part of the heat conduction path between the heat source and sink.

To minimize contact thermal resistance (R_c) between the nanowire and suspended membranes, a wetting procedure was applied after the nanowire was placed onto the device. Reagent alcohol was locally applied onto the membranes and then the device was heated up to ~80°C to allow for evaporation of the liquid. The evaporation process can strengthen the binding between the sample and membranes and therefore reduce R_c[24]. As shown in Fig. 2a in the main text, negligible contact thermal resistance was achieved with the wetting treatment. For all measured samples, negligible R_c was achieved as evidenced by the overlapping thermal conductivities of the same bare wire measured at different suspended lengths.

Uncertainty analysis
The measured thermal conductivity κ is calculated as

$$\kappa = \frac{GL}{A}, \tag{S3}$$

where G is the measured thermal conductance, L is the measured suspended length of the SiC nanowire, and A is the wire cross-sectional area. The uncertainty for κ is determined by

$$\frac{\delta\kappa}{\kappa} = \sqrt{\left(\frac{\delta G}{G}\right)^2 + \left(\frac{\delta L}{L}\right)^2 + \left(\frac{\delta A}{A}\right)^2}. \tag{S4}$$

The uncertainty of thermal conductance is estimated to be 2-3% depending on temperature, determined using a Monte Carlo approach the same as done in our previous work.[25] The length L is measured by SEM, and the uncertainty is conservatively estimated as 0.2 µm.[23] The cross-sectional area of a nanowire is examined by SEM. We conservatively estimated the uncertainty to be 10%. Based on the uncertainty derived from these sources, the overall uncertainty of the thermal conductivity can be calculated using Eq. (S4), which is determined to be 10.3% at 300 K for Sample S1.

The SPhP thermal conductance is defined by

$$G_{SPhP} = G_{Au} - G_{Bare}, \tag{S5}$$

The uncertainty for G_{SPhP} is given by

$$\delta G_{SPhP} = \sqrt{(\delta G_{Au})^2 + (\delta G_{Bare})^2}, \tag{S6}$$

We then use Eq. (S4) to calculate the uncertainty of κ_{SPhP}. At 300 K, the uncertainty of κ_{SPhP} is 18.5% for Sample S1, which is equivalent to ±1.08 W/m-K.

Thermal conductance enhancement is defined as

$$E = \frac{G_{\text{SPhP}}}{G_{\text{Bare}}}, \tag{S7}$$

The uncertainty is given by

$$\frac{\delta E}{E} = \sqrt{\left(\frac{\delta G_{\text{SPhP}}}{G_{\text{SPhP}}}\right)^2 + \left(\frac{\delta G_{\text{Bare}}}{G_{\text{Bare}}}\right)^2}, \tag{S8}$$

For Sample S1, the uncertainty for thermal conductance enhancement is 15.6% at 300 K.

Thermal data summary

Thermal measurements of the same wire for more than 8 times are extremely challenging. As such, multiple samples were lost during the sample preparation process. In this study, we measured over 21 samples with a total of ~160 times measurements. Table S1 and Table S2 summarize the geometrical information and measurement specifications of all measured samples. 10 samples were measured with Au coating(s) while the other 11 samples were lost/damaged during Au coating process. Thermal data for all Au-coated samples are shown from Fig. S6 to S15 and discussed below.

Data for Sample S2 are partly shown in Fig. 4h in the main text. The sample was measured three times (two different lengths without Au coating and one length with Au coating). The overlapping thermal conductivities of bare wires in Fig. S6a indicates negligible contact thermal resistance. The lattice thermal conductivity in Fig. S6b is smaller than the corresponding value of Sample S1 as shown in Fig. 2. The difference is most likely induced by the structure difference. As shown in Fig. 4e, Sample S2 has a high stacking fault density, which can pose additional resistance to phonon transport.

Data for Sample S3 are summarized in Fig. S7. The overlapping thermal conductivities in Fig. S7a indicate negligible R_c for all the measurements, which is confirmed by the resistance data in Fig. S7b with a linear length dependence extrapolating to the original point. Measurements with Au coating at one end were performed at two different lengths. The room temperature enhancement is 9.2% for a suspended length of 21.3 μm and 14.3% for a suspended length of 11.0 μm, corresponding to a SPhP thermal conductivity of 0.7 W/m-K and 2.0 W/m-K, respectively.

Fig. S8 shows the data for Sample S4. The bare wire was measured at four different lengths to confirm the negligible R_c (Fig. S8a). Measurements with Au coating at one end were performed at four lengths, resulting in a room temperature enhancement ranging from 1.8% to 12.7% and a SPhP thermal conductivity from 0.4 W/m-K to 3.1 W/m-K as the suspended length reduces. The extracted G_{SPhP} in Fig. S8d demonstrates that the propagation decays exponentially with length. The extracted pre-decay thermal conductance (G_0) also follows a T^2 temperature dependence below 60 K. The extracted decay length (Fig. S8f) decreases as the temperature increases in the low temperature regime and then flattens above 100 K.

Data for Sample S5 are summarized in Fig. S9. No contact thermal resistance was observed during the measurements. With a suspended length of 46.2 μm, the room temperature enhancement is 1.9% with a SPhP thermal conductivity of 0.5 W/m-K. The sample got damaged after the measurement with Au coating at 46.2 μm suspended length but it should demonstrate a similar level of SPhP thermal conductivity as Samples S1, S3 and S4.

Data for Sample S6 are summarized in Fig. S10. No contact thermal resistance was observed at two different suspended lengths. With a suspended length of 46.4 μm, thermal measurements with

Au coating on one end and both ends were performed. The measured total thermal conductivity shows a clear increase (Fig. S10b), as we introduce the Au launcher into the system. The enhancement for coatings on both ends is approximately doubled compared to that with Au coating on one end. The room temperature enhancement is 2.4% and 4.9% with a SPhP thermal conductivity of 0.6 W/m-K and 1.2 W/m-K, respectively. The sample got damaged after the measurement with Au coating at 46.4 μm but it should demonstrate a similar level of SPhP thermal conductivity as Samples S1, S3, S4, and S5.

Fig. S11 and Fig. S12 depict the thermal properties of Sample S7 and S8, respectively. Overlapping thermal conductivities in both figures for bare wires of different suspended lengths indicate negligible contact thermal resistance. With a suspended length of ~12 μm, the room temperature enhancement is 5.2% with a SPhP thermal conductivity of 1.2 W/m-K for Sample S7 and 1.8% and 0.4 W/m-K for Sample S8 at the shortest measurement lengths. The SPhP-mediated thermal conductivity, while discernible, is lower than that for Samples S1, S3, S4, S5, and S6, indicating higher stacking fault density in these two wires.

Data for Sample S9 and S10 are summarized in Fig. S13 and S14. The two samples were measured with Au coating at four suspended lengths. The thermal conductivity enhancement increases as suspended length reduces. The highest room temperature enhancement is 3.7%, corresponding to a thermal conductivity of 0.8 W/m-K for Sample S9. The enhancement is even smaller for Sample S10. The room temperature enhancement is only observable at the shortest length, indicating a stronger decay process. Note that even with the strong decay, no negative impact to the lattice thermal conductivity that is beyond measurement uncertainty can be observed.

Fig. S15 summarizes the thermal results at 300 K with Au coating. Enhancement level varies among samples. About one half samples (5 out 10) demonstrate significant enhancement with a maximum enhancement over 21% at a ~11.8 μm suspended length with both ends coated with Au, which gives a SPhP thermal conductivity of 5.8 W/m-K.

In addition, to verify the origin of the thermal enhancement with the Au pad, we conduct an experiment to see whether there is thermal rectification when the Au pad is placed on the cold side only. As shown in Fig. S16, we first measured a sample with the Au-coated wire segment placed on the hot side and observed the thermal conductivity enhancement with respect to the value for the same uncoated bare wire. Then we switched the heating and sensing side for the same sample with the Au pad now sitting on the sensing/cold side. The results show that when the Au pad is placed on the sensing side, we also observed similar thermal conductivity enhancement (Fig. S16b).

The reason for the lack of thermal rectification is that phonon polaritons are thermally launched no matter whether the Au-coated segment is placed on the hot or cold side. While the phonon polaritons emitting from the Au pad are out of thermal equilibrium with the conduction channel, i.e., the suspended bare SiC nanowire segment, they are thermally launched at the interface between the SiC nanowire and Au coating that sits on the membrane. As such, the phonon polaritons launched from each membrane are in thermal equilibrium with the membrane from which they are launched. Now when the Au pad is placed on the cold side with a lower temperature, the average energy of the phonon polaritons are lower than the average energy of the phonons on the hot side. As such, the incoming phonon polaritons from the cold side help reduce the temperature of the hot side. The net effect of this process is equivalent to moving phonon polaritons away from the high temperature side when the Au pad is placed on the hot side. Therefore, the

thermal conductivity of the nanowire is enhanced regardless of whether the Au coated portion is on the hot or cold side.

At elevated baseline temperatures (> 80 K), the level of enhancement with the Au pad sitting on the hot or cold side is approximately the same, as shown in Fig. S16c,d. This is because the temperature difference between the hot and cold membranes during the measurement (~2-3 K on average) is much smaller than the baseline temperature. Interestingly, however, as the temperature drops below 80 K and the temperature difference between the two membranes becomes more important as compared to the baseline temperature, we do notice a difference resulting from where the SPhPs are launched. It is expected that more SPhPs are launched when the Au pad is sitting on the hot side; and therefore, the magnitude of thermal conductivity enhancement when the Au pad is placed on the hot side is higher than that when the Au pad is on the cold side, and this difference becomes more significant as the baseline temperature becomes lower, as shown in Fig. S16d.

Additional optical results

Additional optical results for the two samples in Fig. 4 (Sample S1 and S2) in the main text are shown in Fig. S17-S19. s-SNOW mappings at different frequencies of Sample S1 (Fig. S17) and Sample S2 (Fig. S19) are consistent with the data in the main text.

For nano-spectroscopy (nano-FTIR) of individual 3C-SiC nanowires on the substrate, the sample was illuminated by a *p*-polarized broadband mid-infrared laser via difference frequency generation (Toptica). The broadband mid-infrared laser was used in the 610 - 1400 cm^{-1} spectral range for all measurements, which covers the full Reststrahlen band of 3C-SiC nanowires. We recorded a nano-FTIR spectrum at each pixel of a line scan along the long axis of a 3C-SiC nanowire with 20 nm spatial resolution. The detector signal was demodulated at frequencies of 2Ω and above, and the obtained spectra were normalized to that obtained in a silicon sample (flat near-field response in the spectral region of interest) using the same acquisition parameters. The interferogram resolution was set to 2048 pixels, and the integration time of each pixel was set to 10 ms. The resolution of each spectrum was set to 6.25 cm^{-1}, corresponding to a moving mirror displacement of 800 μm with the center at 400 μm. The nano FTIR results for Sample S1 shown in Fig. S18 demonstrate the dispersive nature of SPhPs in our SiC nanowire.

Finite element method (FEM) simulations were performed in CST studio suite 2018 for a long 3C-SiC nanowire with one end coated with Au. The entire structure is placed in the vacuum with a *p*-polarized plane wave excitation, which illuminates the entire structure at an angle perpendicular to the long axis of the 3C-SiC nanowire. The temperature-dependent dielectric function used for 3C-SiC was derived from literature[58]. Tabulated dielectric function of gold was used in the simulations, which is shown in Fig. S20[59]. Simulation results in Fig. S21 indicates Au coating can efficiently launch SPhPs at different temperatures (65 nm diameter, 100 μm long SiC nanowire with 30 nm thick, 4 μm long Au pad). Simulation results in Fig. S22 show that as coating length increases, more SPhPs are coupled into the nanowire (60 nm diameter, 44 μm long SiC nanowire with 10 nm thick Au pad).
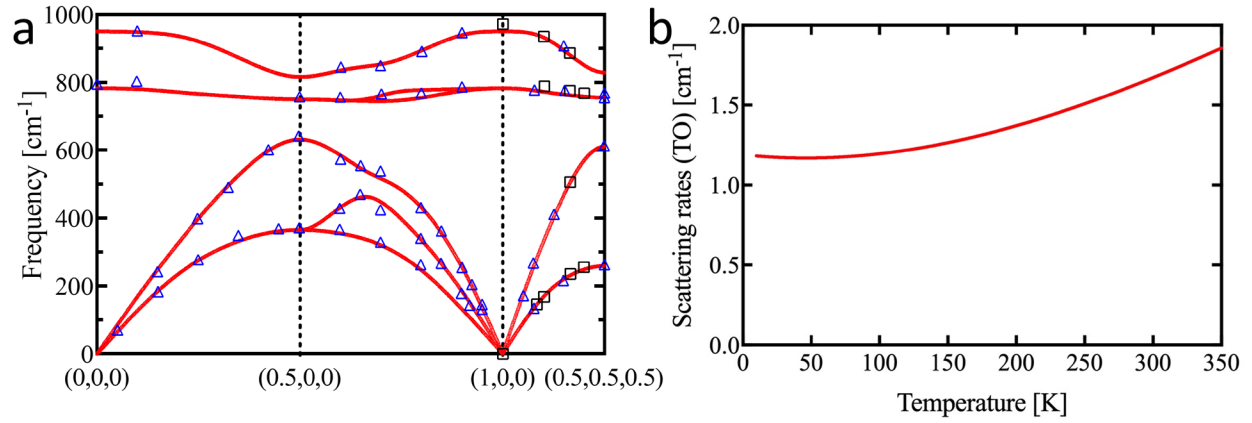
Fig. S1. Phonon dispersion and scattering rates. **a**, Phonon dispersion from first-principles calculations (red curves) compared with inelastic x-ray scattering data[47] (blue triangles) and Raman data[48] (black squares). **b**, Scattering rates for transverse optical (TO) phonon modes as a function of temperature.
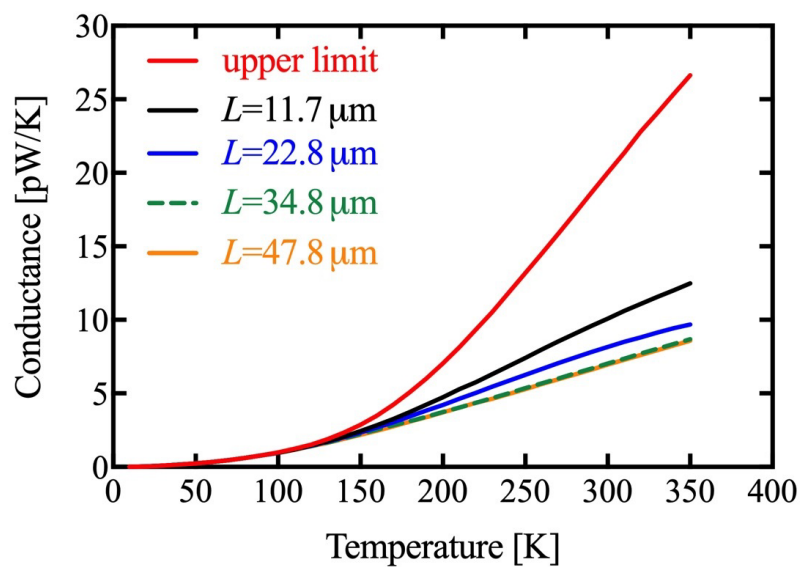
Fig. S2. Calculated thermal conductance as a function of temperature for different sample lengths. The upper limit is obtained for a maximum frequency of infinity achieved using a numerically large number of ω_{max}=53,000 cm^{-1}.
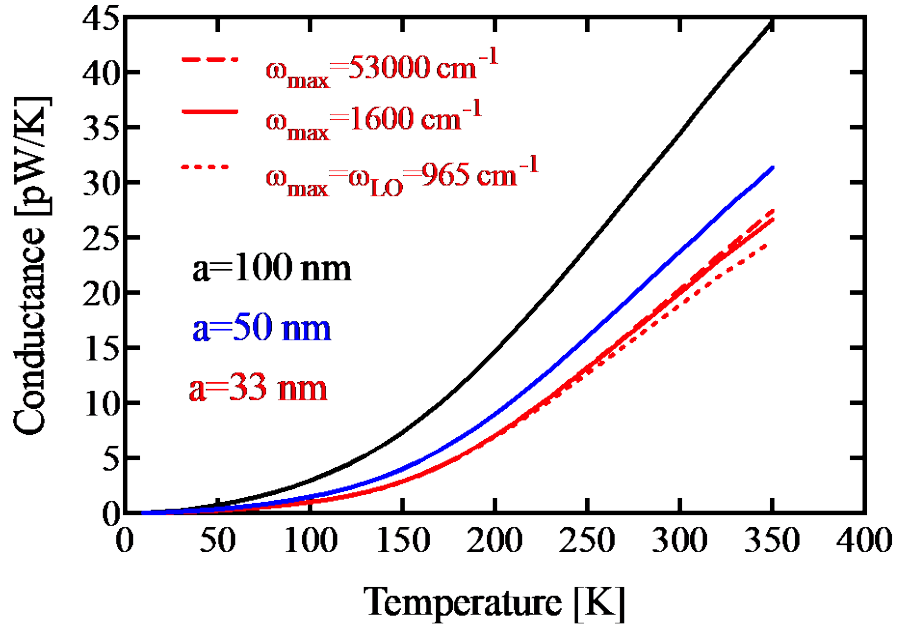
Fig. S3. Calculated upper limit of SPhP conductance for different maximum frequencies in integration as a function of temperature for a SiC nanowire with radius a=33 nm (red curves). The conductance for radii of 50 and 100 nm using ω_{max}=1600 cm^{-1} are also shown.
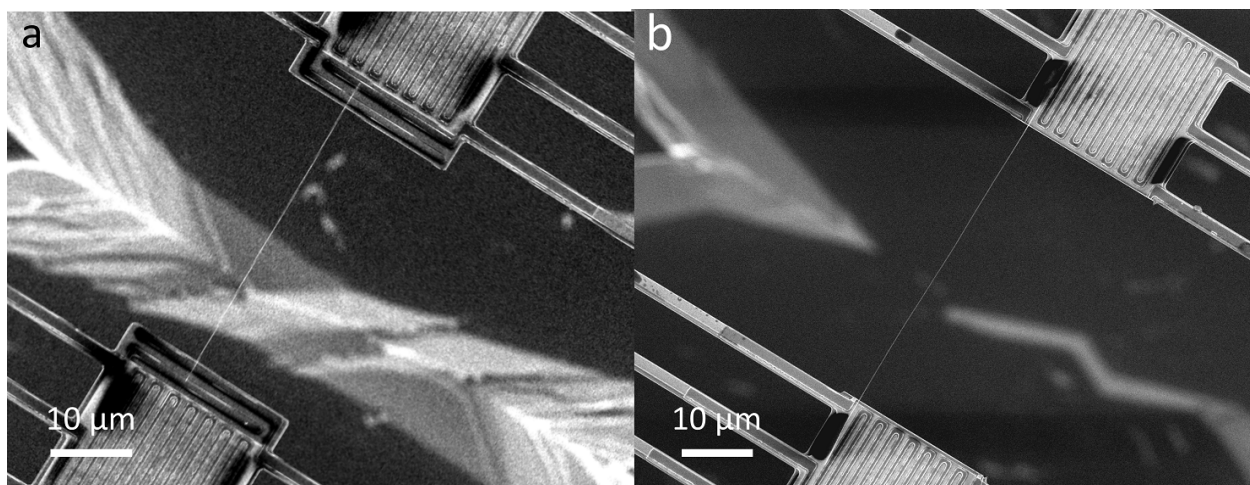
Fig. S4. SEM images of a measurement device **a**, before and **b,** after cutting the extra Pt electrodes.
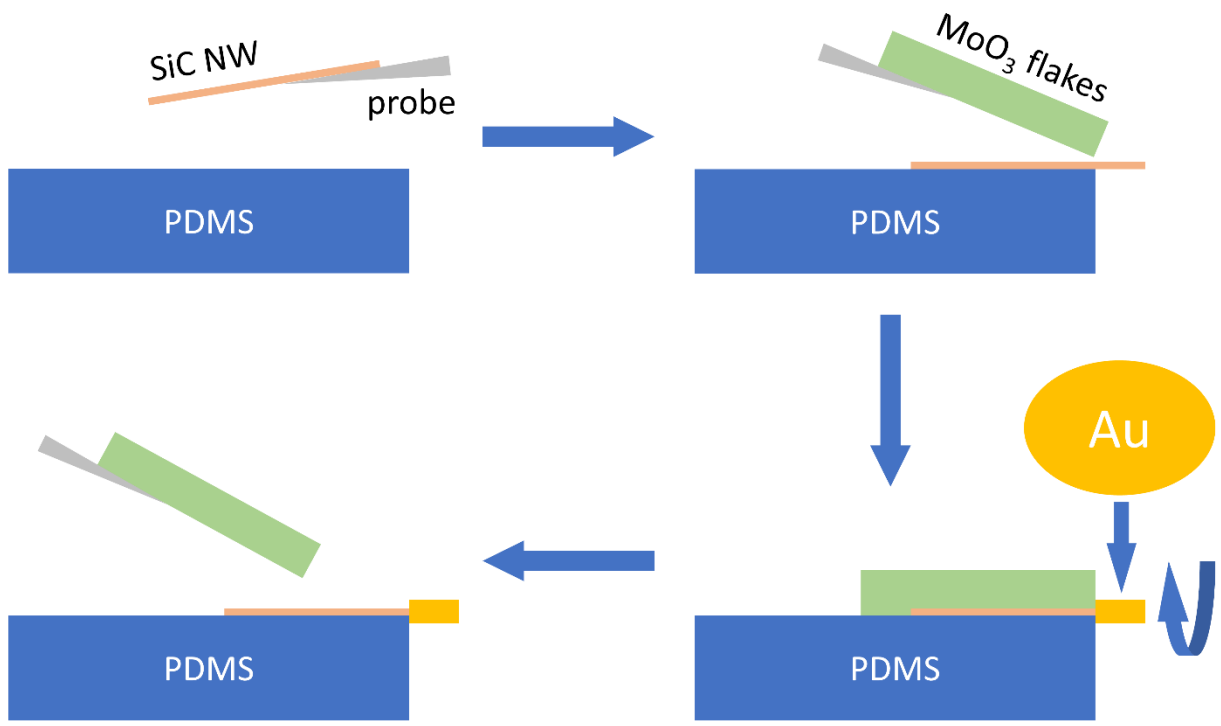
Fig. S5. Schematic illustrations of the Au coating procedure.
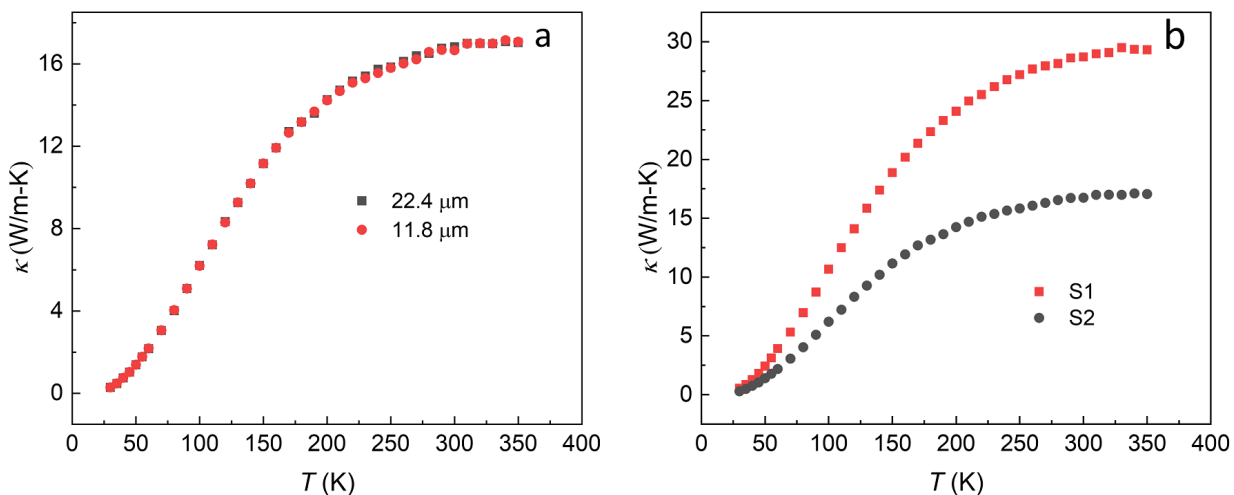
Fig. S6. Additional thermal data for Sample S2. **a**, Overlapping bare wire thermal conductivity at different lengths. **b**, Lower phonon thermal conductivity compared to Sample S1. The two samples have similar diameters (65.5 nm and 65.7 nm) so the lower thermal conductivity for Sample S2 is likely a result of a higher density of stacking faults.
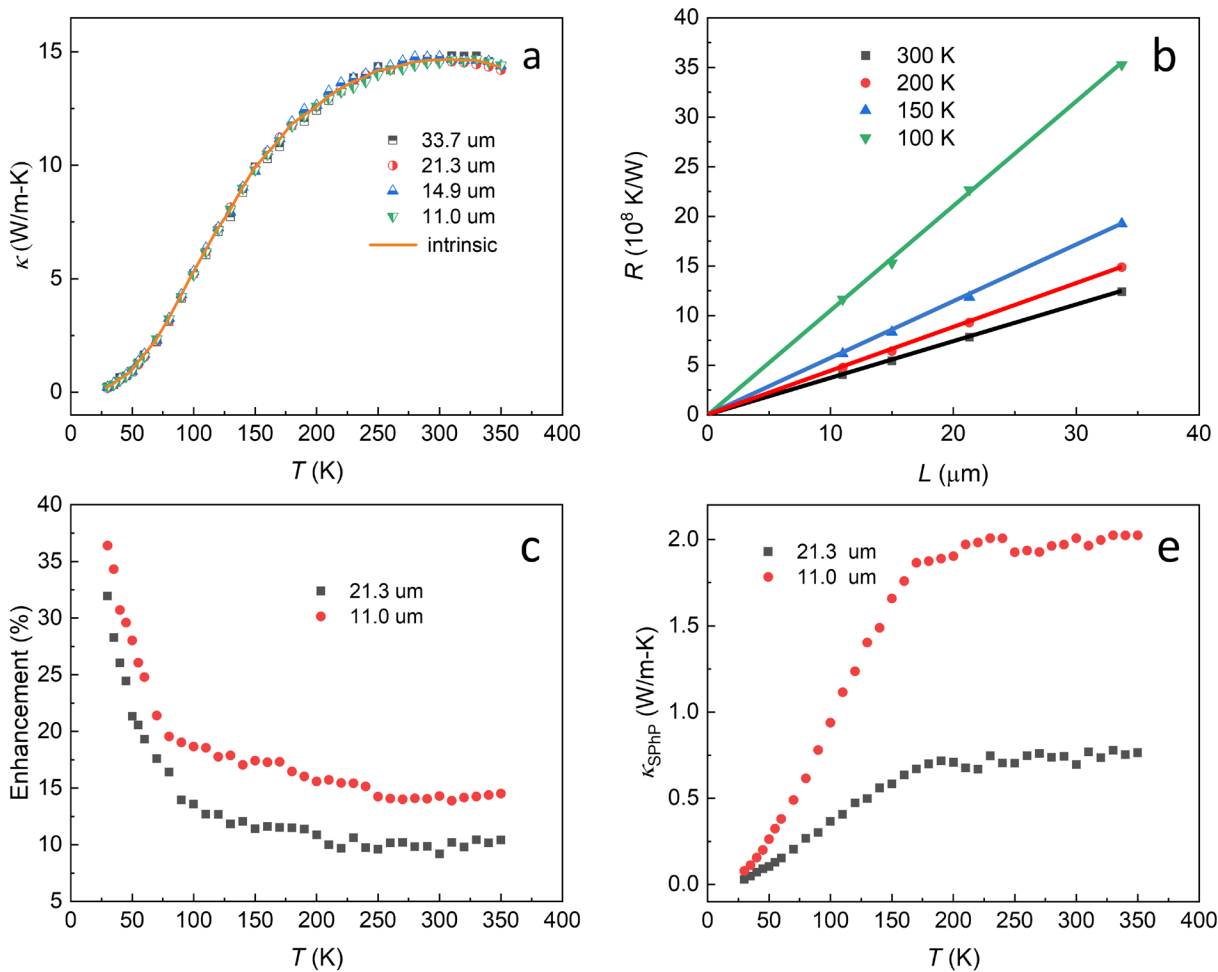
Fig. S7. Thermal data for Sample S3. **a**, Overlapping bare wire thermal conductivities for different suspended wire lengths. **b**, Thermal resistance with respect to length. **c**, Percentage enhancement and **d**, SPhP thermal conductivity at different lengths. The sample hydraulic diameter is 47.3 nm.
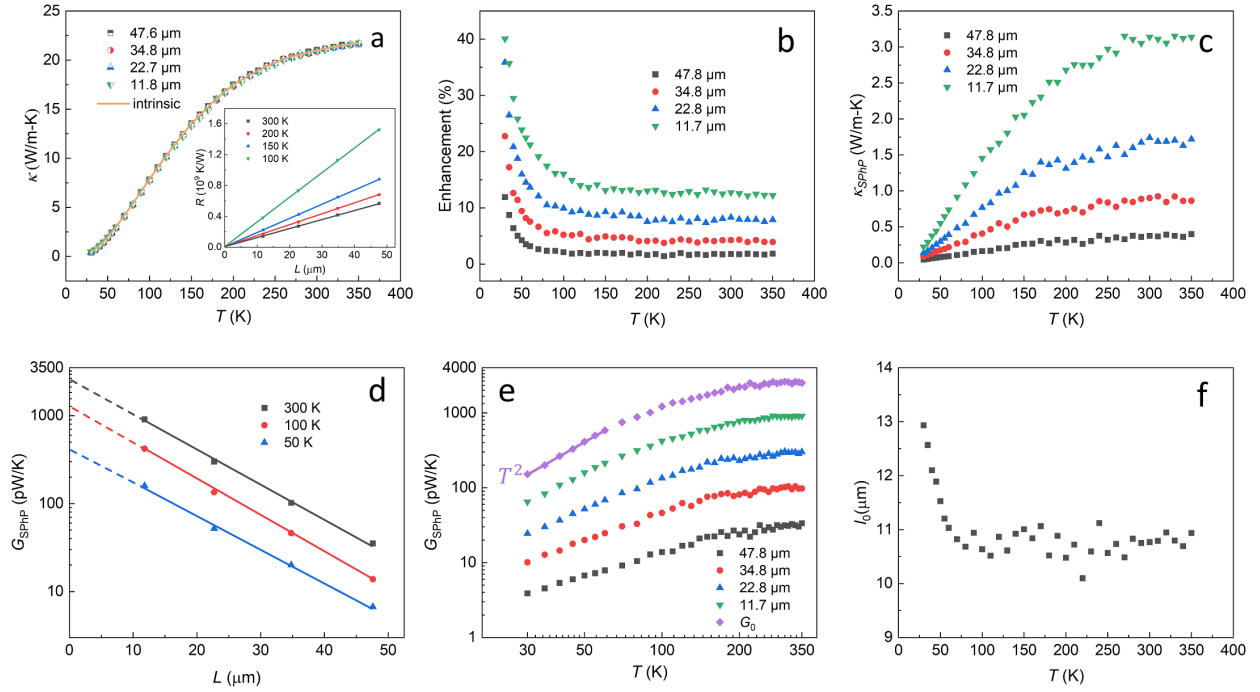
Fig. S8. Thermal data for Sample S4. **a**, Overlapping bare wire thermal conductivities for different suspended wire lengths. Inset: thermal resistance with respect to length. **b**, Percentage enhancement and **c**, SPhP thermal conductivity at different lengths. **d**, Length dependence and **e**, temperature dependence of SPhP thermal conductance. **f**, Extracted decay length. The sample hydraulic diameter is 67.8 nm.
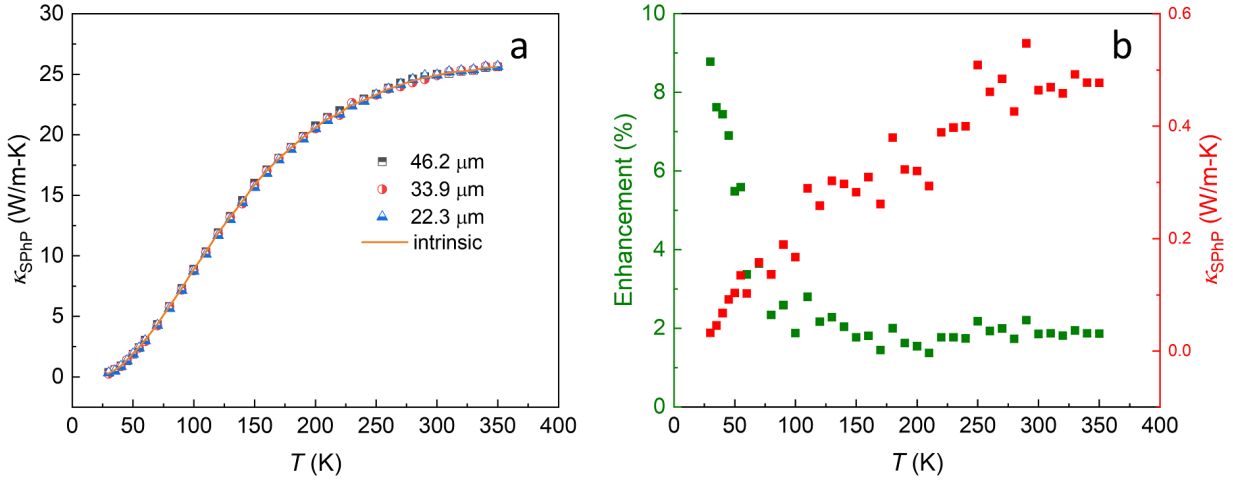
Fig. S9. Thermal data for Sample S5. **a**, Overlapping bare wire thermal conductivities for three different suspended wire lengths. **b**, Percentage enhancement and SPhP thermal conductivity at 46.2 μm suspended wire length. The sample hydraulic diameter is 60.6 nm.
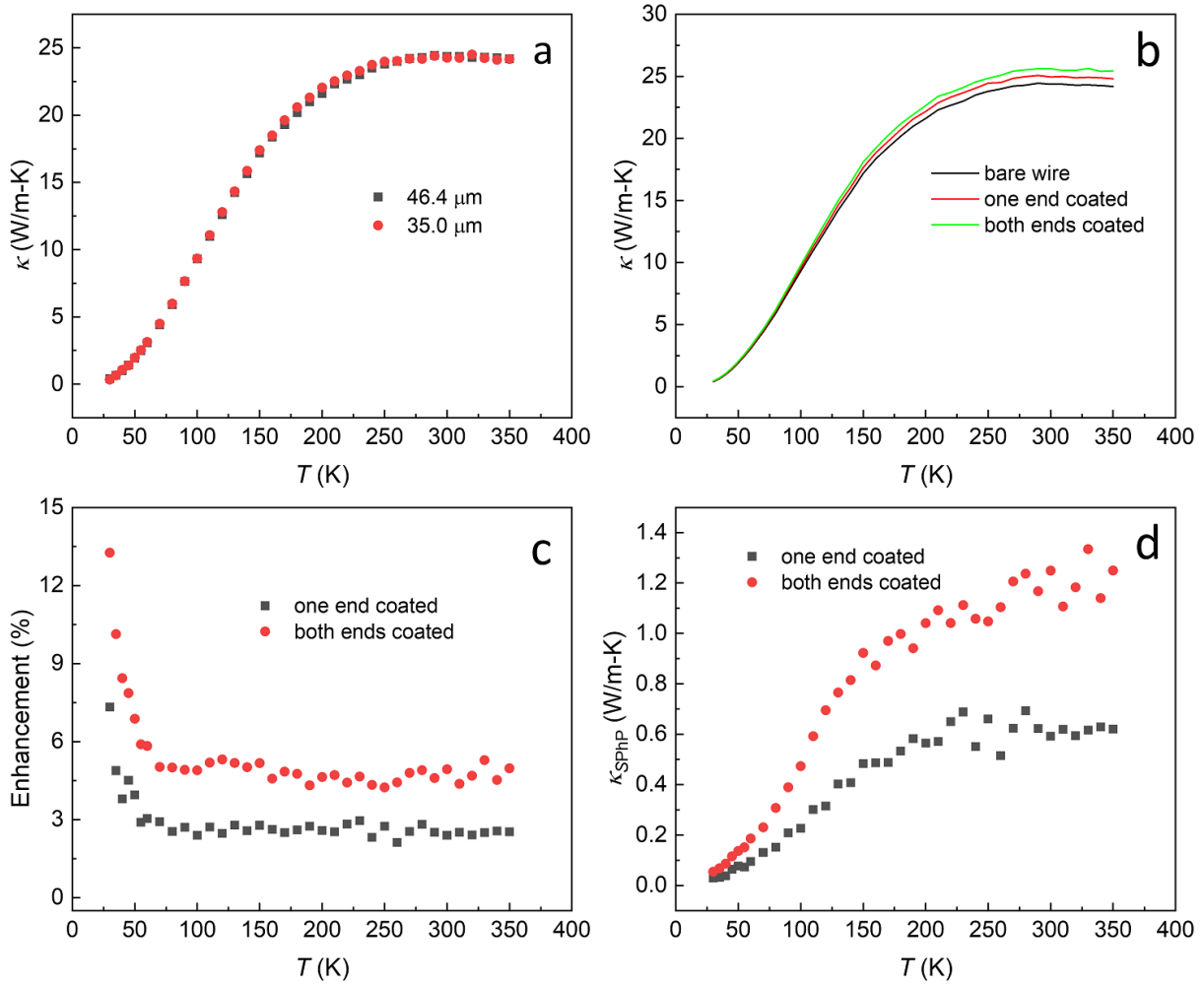
Fig. S10. Thermal data for Sample S6. **a**, Overlapping bare wire thermal conductivities at different suspended wire lengths. **b**, Measured total thermal conductivities of the same wire with and without Au coating at approximately the same suspended length of 46.4 µm. **c**, Percentage enhancement and **d**, SPhP thermal conductivity with different Au coating lengths for 46.4 µm suspended length. The sample hydraulic diameter is 53.8 nm.
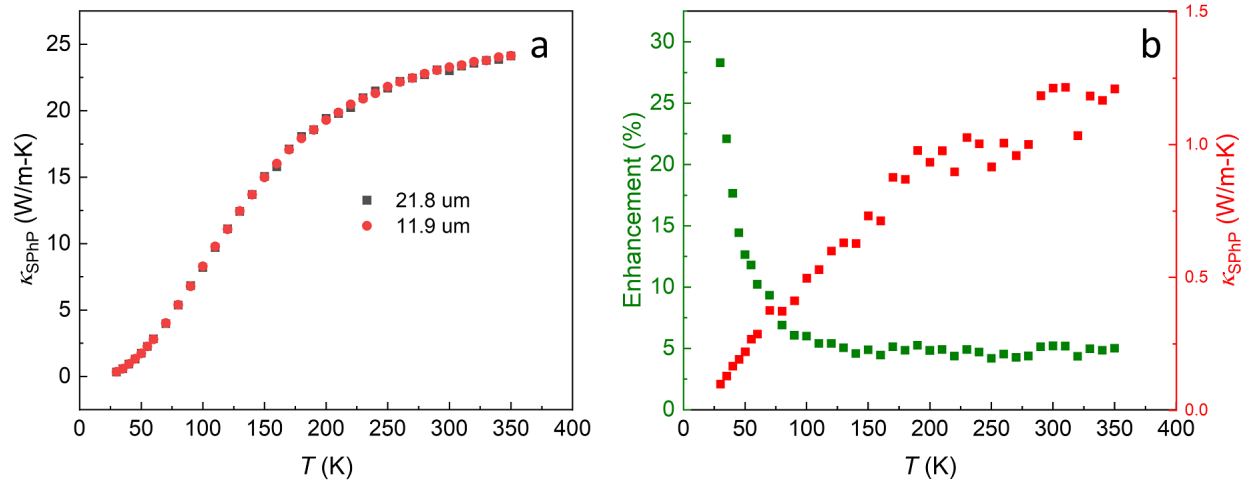
Fig. S11. Thermal data for Sample S7. **a**, Overlapping bare wire thermal conductivities at different suspended wire lengths. **b**, Percentage enhancement and SPhP thermal conductivity for a suspended wire length of 11.9 μm. The sample hydraulic diameter is 55.6 nm.
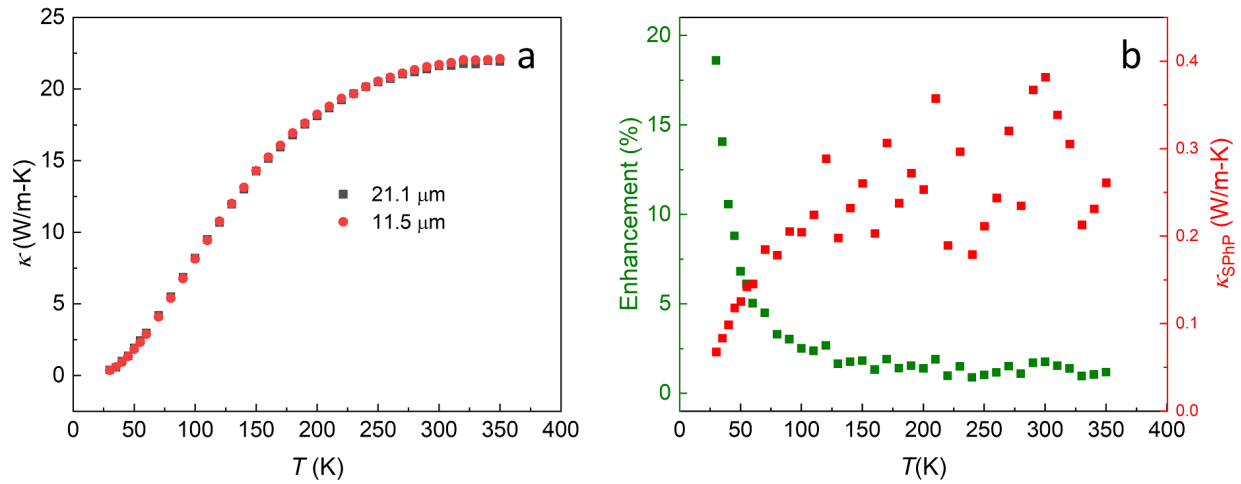
Fig. S12. Thermal data for Sample S8. **a**, Overlapping bare wire thermal conductivities for different suspended wire lengths. **b**, Percentage enhancement and SPhP thermal conductivity for a 11.5 μm long suspended wire length. The sample hydraulic diameter is 69.2 nm.
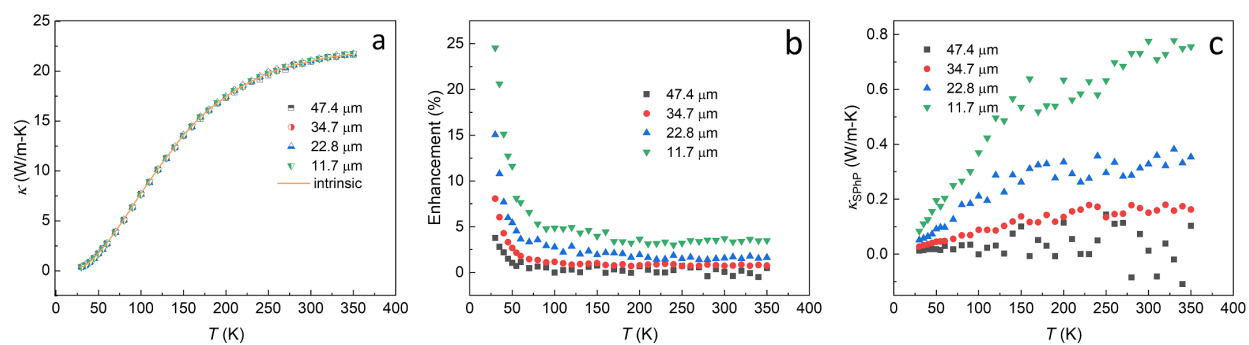
Fig. S13. Thermal data for Sample S9. **a**, Overlapping bare wire thermal conductivities for different suspended wire lengths. **b**, Percentage enhancement and **c**, SPhP thermal conductivity at different lengths. The sample hydraulic diameter is 60.1 nm.
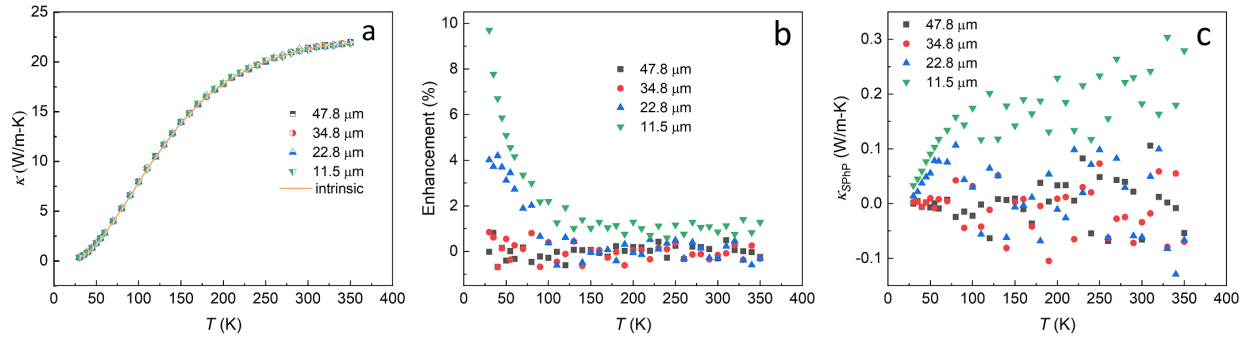
Fig. S14. Thermal data for Sample S10. **a**, Overlapping bare wire thermal conductivities for different suspended wire lengths. **b**, Percentage enhancement and **c**, SPhP thermal conductivity at different lengths. The sample hydraulic diameter is 73.5 nm.
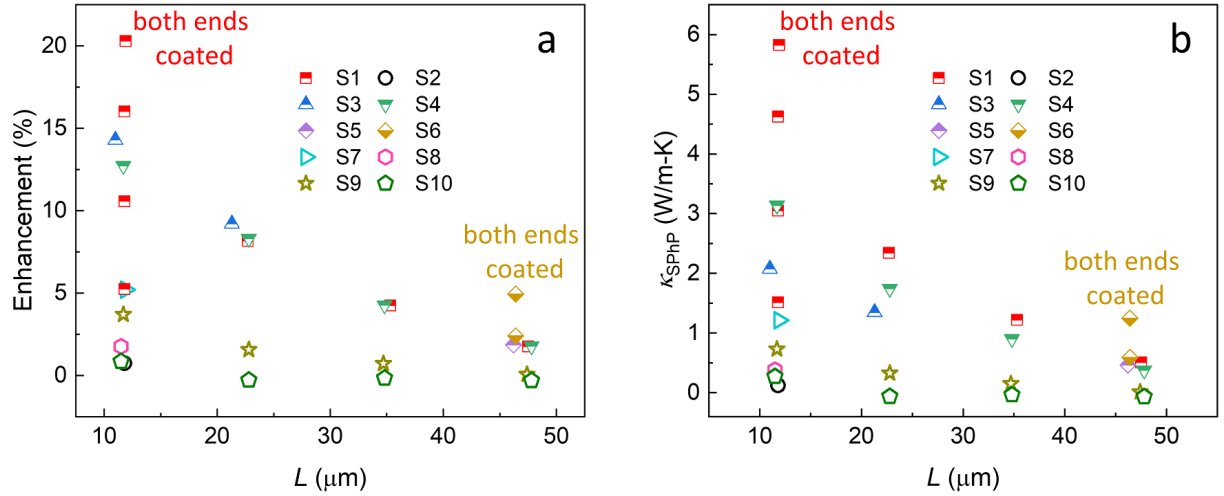
Fig. S15. a, Percentage enhancement and **b**, corresponding SPhP thermal conductivities with Au coating for different samples, different nanowire suspended lengths, and different Au coating lengths at 300 K. Note that for Sample S1, multiple measurements were conducted at an approximately 11.8 μm suspended length with different Au-coating lengths.
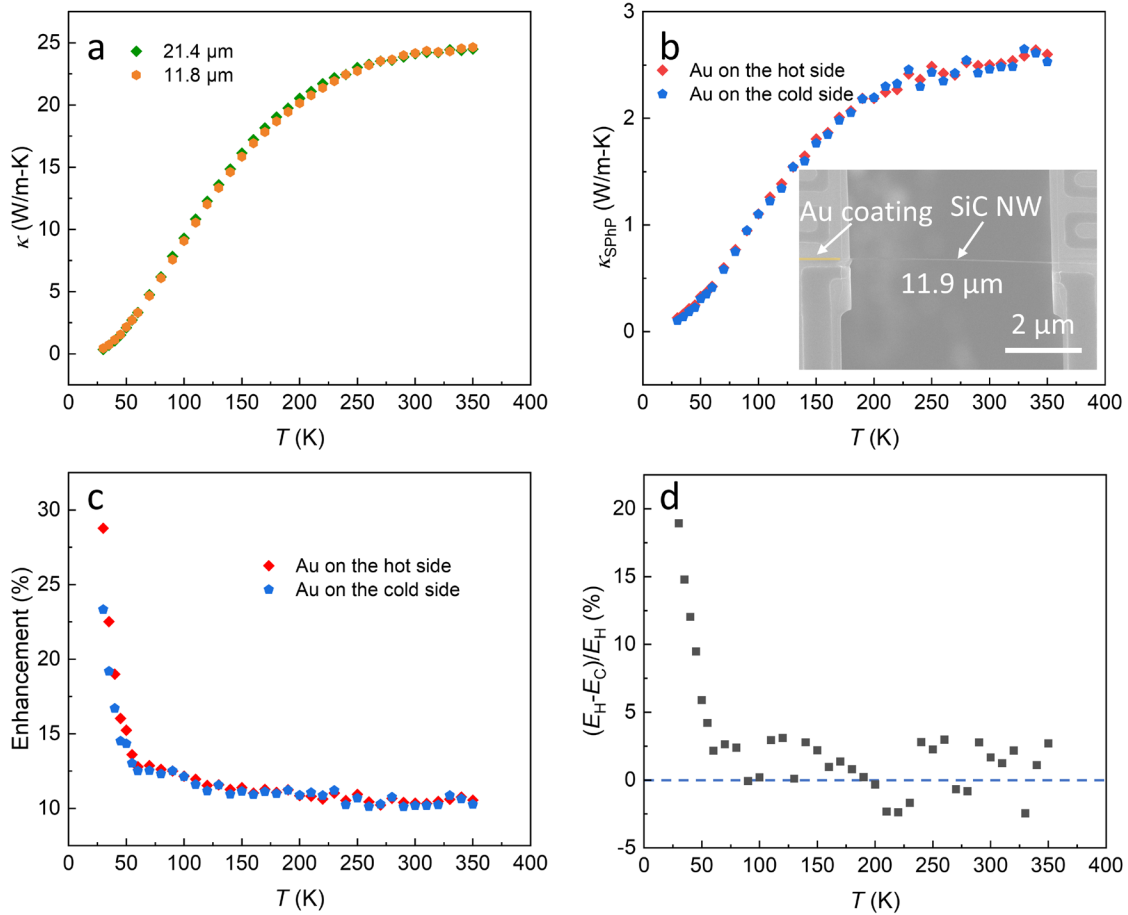
Fig. S16. a, Overlapping thermal conductivity of an uncoated 66.5 nm diameter SiC nanowire at two different suspended lengths, indicating negligible contact thermal resistance. **b**, Extracted SPhP thermal conductivity when the Au coated segment is placed on the hot (red symbols) and cold (blue symbols) side. **c**, Derived percentage enhancement with the Au pad on the hot side (red symbols) and cold side (blue symbols). **d**, Relative difference in the thermal conductivity enhancement with the Au pad placed on the hot side and cold side.
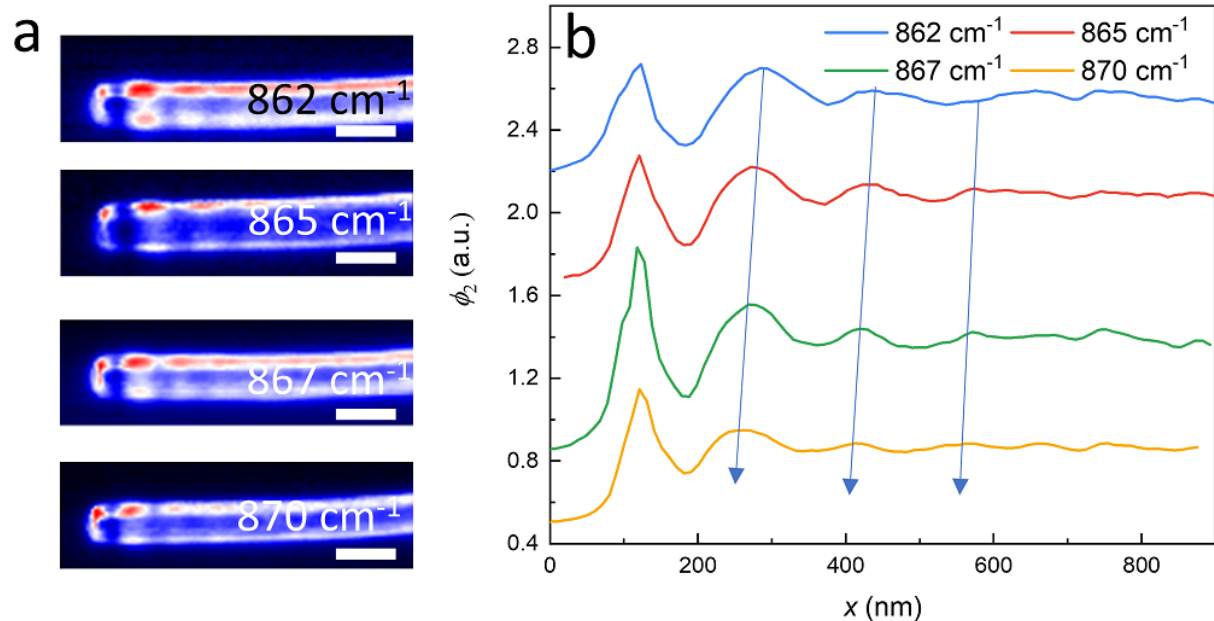
Fig. S17. a, Additional s-SNOM mapping results and **b,** corresponding line profiles at different frequencies for Sample S1. Blue lines are plotted to show the polariton wavelength decreases with frequency increases. The scale bar represents 200 nm.
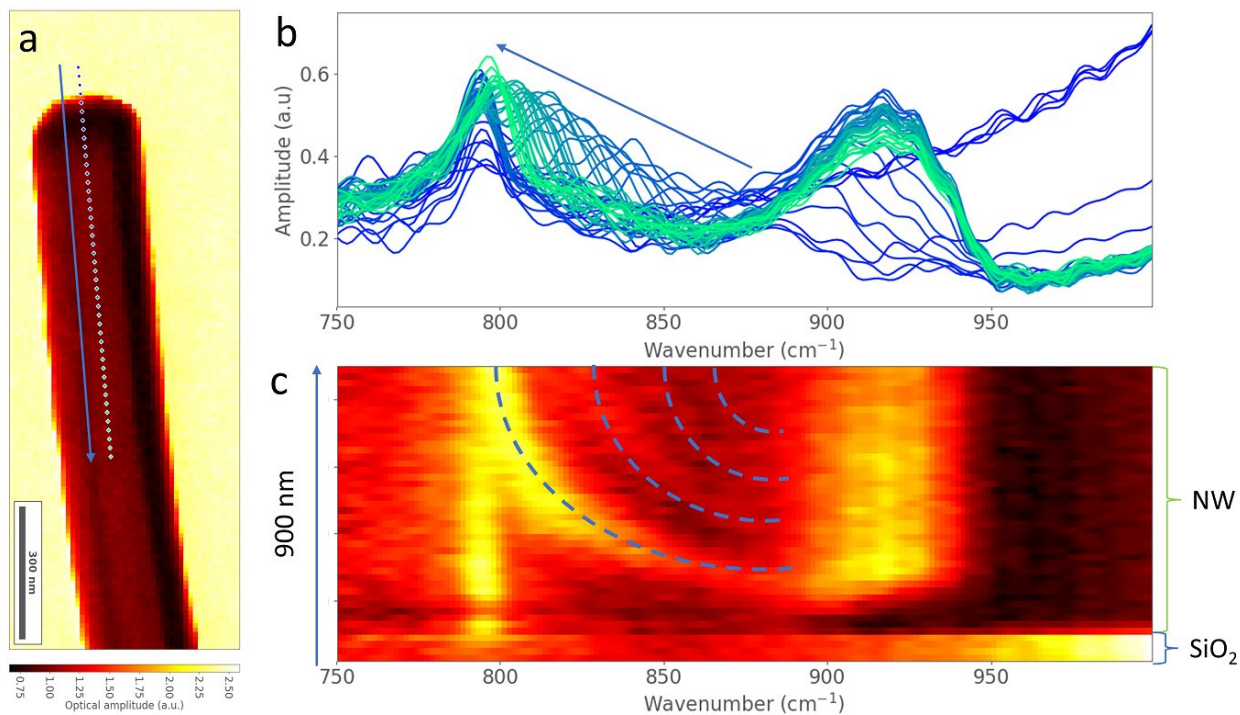
Fig. S18. Nano-FTIR results for Sample S1: **a**, white light IR image, **b**, nano-FTIR spectra recorded at different positions as marked in **a**, and **c**, contour replot of **b**. The white light IR image is the near-field amplitude image, which is spectrally averaged over a range of approximately 610-1400 cm^{-1} by setting the interferometer at the white light position (WLP). Dashed lines (guided to eyes) are plotted in **c** to show SPhPs dispersion in the whole Reststrahlen band of 3C-SiC. Strong near-field resonances near the TO and LO frequencies of 3C-SiC are also observed in the nano-FTIR spectra.
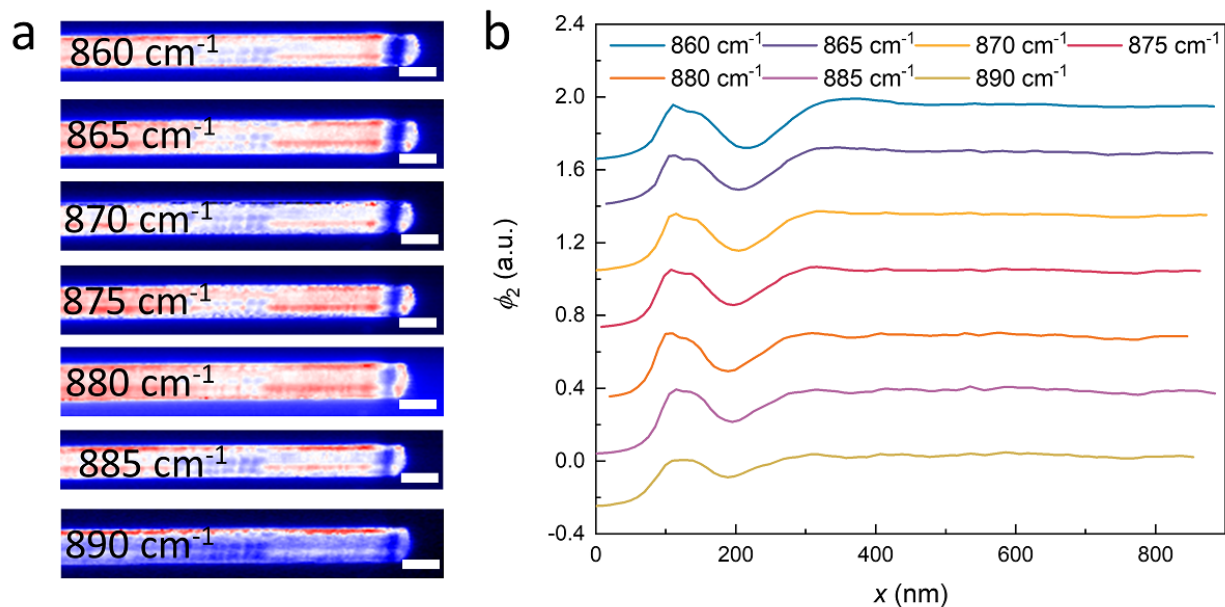
Fig. S19. a, s-SNOM mappings and **b**, corresponding line profiles at different frequencies for Sample S2. The scale bar represents 200 nm.
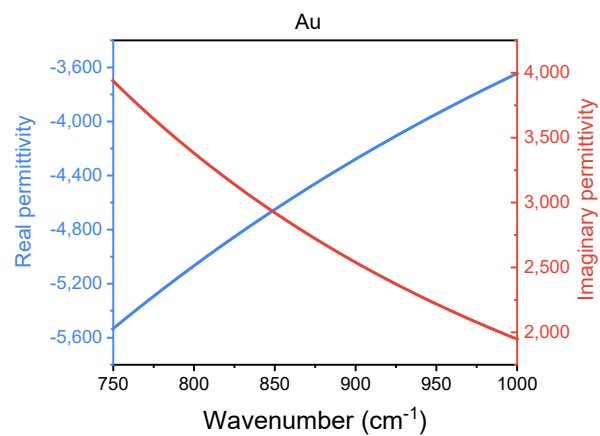
Fig. S20. Dielectric function of gold used in the simulations. Reprinted with permission from Ref. 59. Copyright 2023, John Wiley and Sons.
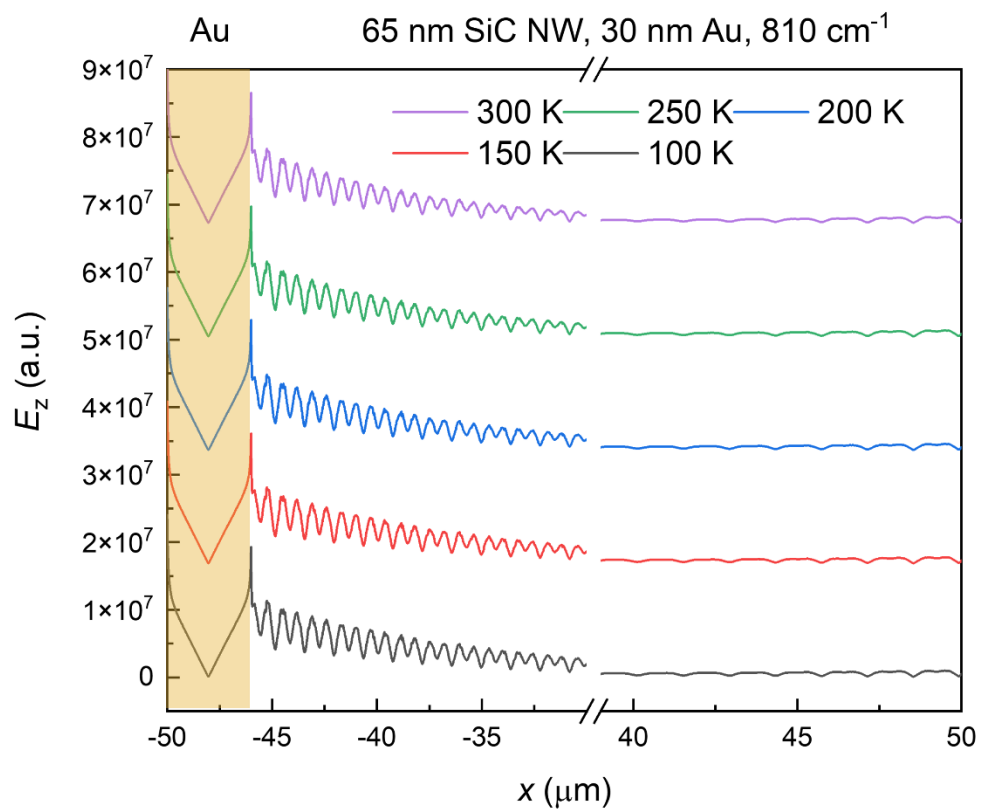
Fig. S21. Simulated electric field (E_z) at 810 cm^{-1} of a 65 nm diameter SiC nanowire at different temperatures with one end coated with 30 nm thick Au.
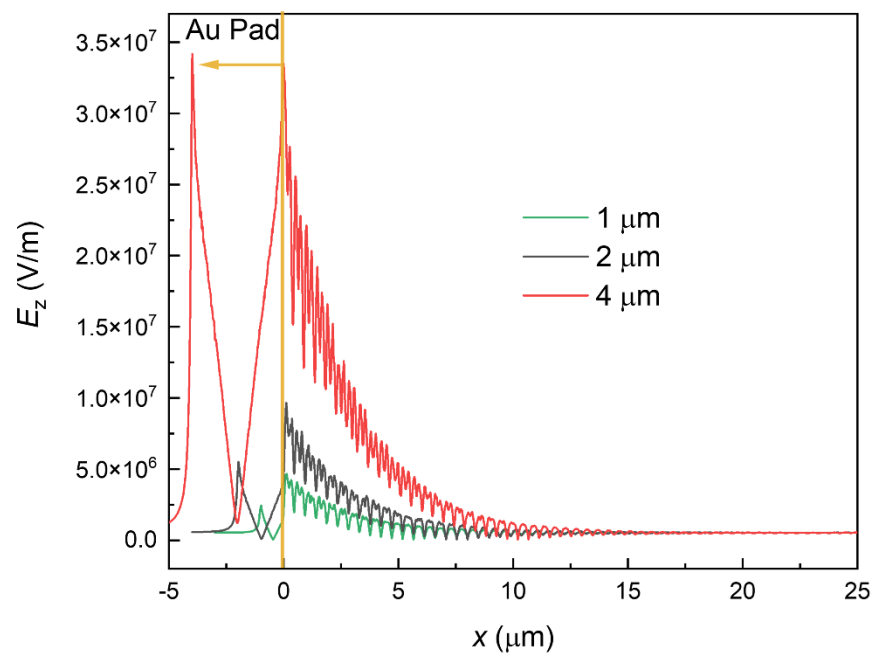
Fig. S22. Simulated electric field (E_z) at 870 cm^{-1} of a 60 nm diameter SiC nanowire at different temperatures with one end coated with 10 nm thick Au pad of 1, 2, and 4 µm long.

Table S1. List of Au coated samples. Here, D_h is the hydraulic nanowire diameter, $L_{suspended}$ is the length of the suspended portion of the nanowire, L_{Au} is the total length of the Au coating on either one or both ends of the nanowire, and κ_{ph} and κ_{SPhP} are the phonon and surface phonon polariton contributions to the total thermal conductivity, respectively.

Sample ID	D_h (nm)	$L_{suspended}$ (µm)	L_{Au} (µm)	$\kappa_{ph,300K}$ (W/m-K)	$\kappa_{SPhP,300K,max}$ (W/m-K)
S1	65.5	47.5/35.3/22.7/11.8/ 11.8/11.8/11.8/11.9	4.8/4.8/4.8/4.8 2.8/4.8/8.0/9.9	28.7	5.8
S2	65.7	11.8	2.7	16.7	0.1
S3	47.3	21.3/11.0	2.8/3.2	14.7	2.0
S4	67.8	47.8/34.8/22.8/11.7	4.1/3.8/4.2/4.2	20.9	3.1
S5	60.6	46.2	3.2	24.9	0.5
S6	53.8	46.4/46.4	4.0/9.7	24.4	1.2
S7	53.0	11.9	4.3	23.1	1.2
S8	69.2	11.5	3.6	21.7	0.4
S9	60.1	47.4/34.7/22.8/11.7	4.4/4.1/4.2/4.1	21.5	0.8
S10	73.5	47.8/34.8/22.8/11.5	4.6/4.6/4.6/4.7	21.4	0.2

Table S2. List of samples without Au coating being performed

Sample ID	D_h (nm)	$L_{suspended}$ (µm)	$\kappa_{ph,300K}$ (W/m-K)
S11	55.6	21.2/15.6/11.6	21.4
S12	76.9	34.2/22.1/15.7	29.1
S13	63.2	34.3/20.7	25.5
S14	63.7	45.0/34.2	24.5
S15	53.8	46.5	23.3
S16	60.1	46.9/35.2	21.6
S17	77.0	47.4/33.5	21.4
S18	53.3	21.5/11.8	15.5
S19	51.2	22.3/11.9	22.3
S20	56.7	22.5/11.9	19.6
S21	62.4	22.3	18.8

Supplementary information references

58. Tong, Z., Liu, L., Li, L. & Bao. H. Temperature-dependent infrared optical properties of 3C-, 4H- and 6H-SiC. *Phys. B: Condens. Matter* **537**, 194-201 (2018).

59. Lu, G. et al. Launching and manipulation of higher-order in-plane hyperbolic phonon polaritons in low-dimensional heterostructures. *Adv. Mater.* **35**, 2300301 (2023).